8/5-23-82

Conf-820930--10

UCRL-87948
PREPRINT

MASTER

TMX TANDEM-MIRROR EXPERIMENTS AND THERMAL-BARRIER THEORETICAL STUDIES

T. C. Simonen, D. E. Baldwin, S. L. Allen, W. L. Barr, et al
Lawrence Livermore National Laboratory, University of California
Livermore, CA 94550 USA

W. L. Hsu, Sandia National Laboratory, Livermore, CA 94550 USA
G. A. Hallock, Rensselaer Polytechnic Institute, Troy, NY USA
O. T. Strand, Johns Hopkins University, Baltimore, MD USA
K. Audenaerde, University of Wisconsin, Madison, WI USA
J. F. Howard, A. J. Lichtenberg, M. A. Lieberman
University of California, Berkeley, CA USA

This Paper Was Prepared for Proceedings of
9th International Conference on Plasma Physics
and Controlled Nuclear Fusion Research
International Atomic Energy Agency
Baltimore, MD USA
September 1-8, 1982

July 29, 1982

Lawrence Livermore National Laboratory

JHP

UCRL--87948

IAEA-CN-41/G-1

DE82 020352

TMX TANDEM-MIRROR EXPERIMENTS AND THERMAL-BARRIER THEORETICAL STUDIES

ABSTRACT

This paper describes recent analysis of energy confinement in the Tandem Mirror Experiment (TMX). TMX data also indicates that warm plasma limits the amplitude of the anisotropy driven Alfven ion cyclotron (AIC) mode. Theoretical calculations show strong AIC stabilization with off-normal beam injection as planned in TMX-U and MFTF-B. This paper reports results of theoretical analysis of hot electrons in thermal barriers including electron heating calculations by Monte Carlo and Fokker-Planck codes and analysis of hot electron MHD and microinstability. Initial results from the TMX-U experiment are presented which show the presence of sloshing ions.

1. ANALYSIS OF TMX ENERGY CONFINEMENT

At the previous IAEA conference [1], we reported early results from the TMX experiment. Subsequent experiments confirmed and extended our early conclusions. This paper reports recent analysis of energy confinement experiments.

TMX experiments demonstrated that central-cell ion and electron confinement were improved a hundred-fold over previous single mirror experiments at comparable temperatures. In the core of the plasma, central-cell particle and energy losses were mainly along the magnetic field. The best central-cell particle confinement product was 10^{11} cm^{-3} s. At the plasma edge, radial particle transport and charge exchange were important processes. A summary of a typical global power balance is given in Table I, showing that we are able to account for about 87% of the trapped neutral-beam power.

A detailed analysis of the flow of power between the different particle species and regions of TMX is shown in Fig. 1. The hot end-cell ions, injected by neutral beams, heat end-cell electrons that in turn heat the electrostatically confined central-cell electrons penetrating the end plugs. These electrons both ionize the gas that fuels the central cell and heat the central-cell ions. Our experiments show that in addition to these Coulomb interactions other important processes and effects include: (1) instability heating of the central-cell ions both in the central cell and during their escape through the plugs, (2) higher electron temperatures in the plugs than in the central cell or near the end walls, (3) a halo of cool plasma that reduces end-cell ion losses due to charge exchange on background gas, and (4) central-cell ion radial transport at levels predicted by resonant neoclassical and ion-neutral transport.

TMX experiments also demonstrated isolation of the electrons from the end walls such that the main axial power loss at the end walls was measured to be by central-cell ions escaping the potential barriers. We were able to demonstrate recovery of 67 watts of electrical power at the expected 47% efficiency from a small (12-cm diameter) single stage direct-energy-conversion module. This isolation was achieved by reducing the

plasma density near the end walls to $\sim 10^9$ cm^{-3} as compared to over 10^{13} cm^{-3} in the end plugs.

2. ION MICROSTABILITY

The Drift Cyclotron Loss Cone (DCLC) mode was successfully stabilized under many conditions in TMX. The measured fluctuations [2] usually had the characteristics of the Alfven ion cyclotron (AIC) at the plug ion cyclotron frequency. There were some occasions when the fluctuations appeared DCLC-like or when fluctuations were absent. The ion-cyclotron fluctuations were usually due to AIC in TMX, rather than DCLC as in 2XIIB, because the DCLC drive was weaker in TMX with its radius (measured in gyroradii) twice the radius of 2XIIB. The TMX observations revealed that the warm plasma that stabilized the DCLC mode also limited the amplitude of the AIC mode. Instead of spreading the angular distribution of hot ions, the end plug fluctuations interacted with central-cell ions to damp the instability and produce a source of warm end-plug ions which were subsequently lost along field lines. Figure 2 shows the correlation between the plug diamagnetism (AIC drive) versus the axial ion end loss current (AIC stabilization). This correlation was observed over a wide range of neutral-beam and gas inputs.

TMX end-cell plasmas were produced by injecting neutral beams nearly perpendicularly to magnetic-field lines. The next generation of tandem-mirror experiments has oblique injection of neutral beams, producing "sloshing-ion" distributions. Earlier work [3] described calculations of stability to DCLC and streaming-ion modes for sloshing ion injection. We have recently completed analysis of stability of sloshing ions to the AIC mode.

A simple sloshing-ion distribution is $f(v) = F(v)G(\phi)$, where v is the ion speed, ϕ is the velocity pitch angle with respect to the magnetic field, and $G(\phi) = \exp[-(\phi - \phi_0)^2/2\Delta^2] + \exp[-(\pi - \phi - \phi_0)^2/2\,^2]$. In this pitch-angle distribution G, ϕ_0 gives the neutral-beam injection angle, and Δ gives the pitch-angular width. We take $F(v) = Cv^{2\ell}\exp(-\alpha v^2)$, $\ell = 0, 1, 2, \ldots$.

Figure 3 gives numerical solutions of the AIC dispersion relation [4] for a uniform plasma with cold electrons, showing the stabilizing effect of oblique neutral-beam injection ($\phi_0 < 90°$). The effect is illustrated in Fig. 3(a) by the plots of the instability growth rate, maximized over real wave numbers k, for various pitch-angular widths Δ. The $\Delta = 0$ result indicates that AIC instability is sensitive to $\langle W_\perp/W_\parallel\rangle = \tan^2\phi_0$, the average over the ion distribution of the ratio of perpendicular to parallel energies, and is strongly stabilized for $\langle W_\perp/W_\parallel\rangle \leq 1$, even for a very narrow pitch-angular distribution. The $\Delta \neq 0$ results show that further stabilization occurs when we introduce a spread of pitch angles.

Figure 3(b) shows convective/absolute boundaries on the plane of width Δ versus injection angle ϕ_0. Higher β expands the absolute region at the expense of the convective region. For fixed β the curves in Fig. 3(b) illustrate the stabilizing effect of oblique injection: the width Δ decreases as ϕ_0 decreases.

3. PROPERTIES OF HOT ELECTRONS IN THERMAL BARRIERS

A component of magnetically trapped, energetic electrons sharply increases the effectiveness of a thermal barrier in a tandem mirror by accentuating the barrier-potential dip [3]. To be effective, the hot

electron density at the barrier midplane must approach the local ion density. Description of the steady-state generation of these electrons by electron cyclotron resonance heating (ECRH) required us to consider many topics: (1) ray tracing calculations of the microwave access to the resonance zones, (2) the conditions for stochastic absorption of the microwave power, (3) the fueling of the hot-electron population from the colder electrons including the effects of plasma potentials, (4) the velocity-space evolution of the distribution function and avoidance of runaway electrons, (5) the required ECRH power, (6) the microstability of the resulting distribution functions, and (7) the effect of the hot-electron pressure on the magnetohydrodynamic (MHD) stability of the system as a whole.

3.1. Electron heating

We have used analytic techniques, numerical solutions of mapping equations, and a Monte Carlo simulation code to investigate conditions for stochastic absorption of ECRH power using single and multiple frequencies. For small machines, we find heating to be improved by two waves having a difference frequency equal to the bounce frequency of electrons near the stochastic boundary; this is in agreement with observations in SM-1 [5]. For large machines such as TMX-U and MFTF-B, heating is completely stochastic without requiring multiple frequencies.

Because the heating is stochastic, we use a time-dependent, bounce-averaged Fokker-Planck code with quasilinear diffusion at the fundamental and second harmonic frequencies to model the fueling of a hot-electron group from a cold thermal background and the subsequent velocity-space evolution of the distribution function. The code, which is nonrelativistic in the ion and electron Coulomb scattering, includes relativistic mass shift of the resonance in the microwave diffusion but does not have Doppler broadening of the absorption. It can model heating for localized (strong single-pass absorption) or nonlocalized (cavity) microwave fields. Variation of assumed microwave characteristics controls buildup time scales, the hot-to-cold electron density ratio, and hot-electron anisotropy. For the start-up problem, strong trapping of central cell electrons occurs when the microwave diffusion at the fundamental resonance is large compared to collisional scattering each into the loss cone. This condition can be written as

$$\frac{3}{2} T_s \text{ (keV)} \gtrsim \left[\frac{n_s (10^{11} \text{ cm}^{-3}) \text{ f (GHz)}}{\Delta\theta^2 \, \epsilon_1^2 \text{ (V/cm)}}\right]^2 \equiv \frac{1}{(\chi\Delta\theta)^2} \qquad (1)$$

where T_s and n_s are source temperature, f is the microwave frequency, ϵ_1 is the electric field strength, and density and $\Delta\theta$ is the angular distance in radians between the mirror loss cone angle and the velocity space pitch angle at the magnetic minimum for electrons just turning at the resonance point.

The goals of these calculations are to aid experiments to control electron distribution in thermal barriers and to calculate the self-consistent axial potential profile. In tandem mirrors the plug plasma beta needs to be carried by the bulk of the electrons, rather than by a small runaway population as is adequate for EBT-type devices. Energy control is to be produced by localizing the rf field energy so that energetic electrons have their resonant cyclotron frequency moved out of the

high microwave field region by their relativistic mass shift. This process has been included in Fokker-Planck calculations. Figure 4 shows that runaway is inhibited, and that a fairly broad electron distribution can be generated.

We studied hot-electron distributions as a function of the heating at fundamental and second harmonic resonance for several values of plasma-source temperature, neglecting ambipolar potential. The TMX-U vacuum magnetic geometry was used. The assumed rf-electric fields were ε_1 = 100 V/cm and the index $N_\perp$ = 1 at both fundamental and second harmonic resonance was assumed.

The dependence on χ, as defined by Eq. (1), of the density, mean energy, required rf power, and the fraction of hot electrons is shown in Figs. 5(a) to 5(d). The hot-electron fraction is defined as the number of electrons with energies exceeding 2 keV, the approximate depth of the thermal barrier expected in the TMX-U experiment. Electrons with lower energy would be expelled by the potential.

The plasma energy and density are seen to be increasing functions of χ and central-cell electron temperature, as expected, since rf diffusion becomes strong compared to collisional losses. The saturation in mean-electron energy shown in Fig. 5(b) results from the relativistic detuning of the rf diffusion. The dashed curves are a plot of the strong trapping condition, given by Eq. (1), where V_{rf} is the rf velocity diffusion rate and V_c is the 90° pitch angle scattering frequency.

The rf electric field is an input parameter for the calculation. A value of 100 V/cm produces hot electron density and energy for TMX-U. This value of field is consistent with the available microwave power. The microwave absorption is expected to be strong for Maxwellian plasmas. The localized heating, which limits the energy, should adjust the absorption coefficient, as is manifested in the distortion of the electron velocity distribution, so that absorption and electron losses are in balance.

These calculations do not include the axial potential which is important for the low-energy electrons and provides the thermal barrier. Both a multi-region, finite-element Fokker Planck code and a Monte Carlo code have been recently developed and show that the potential decreases the electron trapping rate.

3.2 Hot electron stability

The hot electrons have magnetic drift frequencies that exceed typical MHD growth rates. As a result, they contribute to the MHD motion only if the β-value omitting hot electrons exceeds the Van Dam-Lee condition [6]. This situation opens options for controlling the system's overall MHD stability by choosing parameters relative to this critical value, depending on whether the hot electrons are in a good- or bad-curvature region.

Adapting the Van Dam-Lee analysis for minimum-B wells, as in TMX-U and MFTF-B, we find that we can use conventional MHD stability anaylsis provided we modify the hot electron beta (β_{he})

$$\beta_{effective} = \beta_{he} \frac{\beta_w}{\beta_w + 2r_p/R_c}$$

where β_w is the beta of the warm non-rigid electrons and ions, r_p is the plug radius, and R_c is the plug radius of curvature.

Microinstabilities with frequencies in the neighborhood of the electron gyrofrequency Ω_e determine the stable operating regime of hot-electron cells. We solve a fully electromagnetic dispersion relation governing longitudinal and transverse waves in a uniform plasma, allowing for oblique propagation. Electron distribution functions are chosen to model the Fokker-Planck code results.

Both the whistler and the upper-hybrid loss-cone (UHLC) modes are found to be potentially unstable. Figure 6 shows the convective-absolute instability boundary of both modes. For TMX-U parameters, hot-electron cells can be free from absolutely unstable whistler and UHLC modes if the temperature anisotropy $\langle T_\parallel \rangle / \langle T_\perp \rangle \geq 0.4$ and $\omega_{ptot}^2/\Omega_e^2 < 1.55$. However, both modes are convectively unstable with the maximum temporal growth rates greater than $0.004\ \Omega_e$ if $\omega_{ptot}^2/\Omega_e^2 \geq 0.55$. Along the convective-absolute instability boundary, the whistler mode propagates in the parallel direction with a spatial growth rate on the order of $(5\ \rho_e)^{-1}$. The spatial growth of the upper-hybrid loss-cone mode is predominantly in the perpendicular direction with a growth rate $\sim(0.5\ \rho_e)^{-1}$.

3.3 Startup calculations

We have evaluated scenarios for the startup of a thermal barrier tandem mirror based on satisfying the following global constraints: particle and power balance for each species in each cell, MHD stability, microstability of both hot ions and hot electrons, and stability to trapped-particle modes. Our startup scenario differs from previous TMX procedures where the plasma was built-up to high density ($\sim 10^{13}$ cm^{-3}) as rapidly as possible in order to be able to maintain the plasma boundary against charge exchange on neutral gas. The hot electron power balance requires that start-up begin at lower density [$<10^{12}$ cm^{-3}] when electron temperatures are low. Then the electrons build-up to full temperature and density over a period of a few tens of milliseconds. Now, rather than sustaining the plasma boundary with neutral beams as previously, it is sustained by warm ions streaming from the central cell and by hot electrons that are mirror trapped in the plugs, much as in the Elmo Bumpy Torus.

Central cell heating with ICRH [7] is planned during thermal barrier startup and operation. Its purpose is to reduce the collisional filling of the barrier due to passing ions from the central cell to a low enough level to be pumped. The major advantage of ICRH is that at Ω_{ci}, the bulk of the ion distribution is directly heated. Neutral beams or ICRH at $2\Omega_{ci}$, on the other hand, indirectly heat the bulk ions through collisions with hot ions. This is less effective at low densities during startup before the formation of a thermal barrier and when the central cell plasma depends on only magnetic confinement with little or no electrostatic enhancement. After thermal barrier formation, we continue the buildup to steady state.

4. INITIAL TMX-U RESULTS

In this section we describe our first results from TMX-U after a few weeks of operation. Machine parameters are listed in Table II. The initial experiments are carried out with 1 MW incident neutral beam power in each end plug and in the central cell. We also carried out experiments with 50 kW ECRH power. The objective of these experiments is to operate in the conventional tandem mirror mode without thermal barriers to get an

early assessment of the system performance. In these early experiments we have generated and measured the angular distribution of hot sloshing ions in the end cells with two arrays of secondary emission detectors which viewed the plasma at the midplane of each plug at various angles. These measurements, shown in Fig. 7(a), show the energetic plasma ions to be peaked in velocity space at 47°, the beam injection angle. The hot ion density increases rapidly with increased beam current. Figure 7(b) shows the axial density profile of hot ions resulting from inverting the angular distribution shown in Fig. 7(a). The absolute hot ion density is uncertain because the hot core radius is uncertain, but is in the range of 10^{12} cm^{-3}.

REFERENCES

[1] T. C. Simonen, et al., Plasma Physics and Controlled Nuclear Fusion Research (Proc. 8th Int. Conf., Brussels, Belgium, 1980) IAEA, Vienna (1980) I, 97.

[2] T. A. Casper and G. R. Smith, Physical Review Letters, 48 (1982) 1015.

[3] D. E. Baldwin, et al., Plasma Physics and Controlled Nuclear Fusion Research (Proc. 8th Int. Conf., Brussels, Belgium, 1980) IAEA, Vienna (1980) I, 97.

[4] J. Scharer, Plasma Phys. II (1969), 1.

[5] N. H. Lazar, et al. Symmetric Tandem Mirror Program Annual Progress Report, TRW Report TRW.82.T620.1-001 (1981).

[6] J. W. Van Dam and Y. C. Lee, in Proc. EBT Ring Physics Workshop, Oak Ridge, TN (1979), p. 471.

[7] B. D. McVey, et al., Bull. Am. Phys. Soc. 26 (1981), 902.

Table I. Global power balance. Net input trapped power 100% (420 kW).

Loss mechanism	Power, %
Axial power loss	35 ± 10
Plug-ion charge exchange on gas	30 ± 15
Fueling losses	15 ± 5
Impurity radiation	7 ± 2
Total	87 ± 27

TABLE II. Comparison of major differences between TMX and TMX-Upgrade.

System	TMX	TMX-Upgrade
Magnet		
End-plug midplane field (T)	1.0	0.5
Plug-mirror ratio	2:1	4:1
Plug length (m)	0.9	3.0
Central-cell length (m)	5.5	8.0
Central-cell field strength (T)	0.1	0.3
Neutral beam		
Maximum power (MW)	5	10
Plug injection angles (deg.)	90	47, 18
Central-cell injection angles (deg.)	90	70, 58.5
Duration (ms)	25	75
ECRH		
Number of 200 kW 28-GHz gyrotrons	0	4
ICRH		
Central-cell power (kW)	--	200

FIGURE CAPTIONS

Fig. 1. TMX Power Flow derived from measured plasma parameters.

Fig. 2. End-cell diamagnetism versus end-loss current.

Fig. 3a. The maximum growth rate of AIC instability, in units of the ion cyclotron frequency, as a function of the neutral-beam injection angle ϕ_0 and pitch-angular spread Δ. The uniform 10 keV deuterium plasma has density 4×10^{12} cm^{-3} and $\ell = 1$, and the magnetic field strength is 10 kG.

Fig. 3b. Convective-absolute boundaries for AIC instability in a uniform 10 keV hydrogen plasma with $\ell = 2$ in a 5 kG field.

Fig. 4. Contour plot of the electron distribution function in midplane phase space showing that localized ECRH inhibits resonant runaway as evidenced by the rapid decrease in electron density at high energy. The distribution function decreases by a factor 0.58 between contours.

Fig. 5. Plots of (a) plasma density, (b) mean electron energy, (c) fraction of hot electrons, and (d) required ECRH power as a function of χ with relativistic detuning. The source (central cell electron) temperature is T_e. Plasma potential is assumed zero.

Fig. 6. Convective-absolute instability boundaries for the whistler mode (solid curve) and the upper-hybrid loss-cone mode (dashed curve). TMX-U can obtain over a range of parameters crossing the convective-absolute boundary.

Fig. 7a. Angular distribution of hot end plug ions in TMX-U.

Fig. 7b. Axial density distribution of sloshing ions.

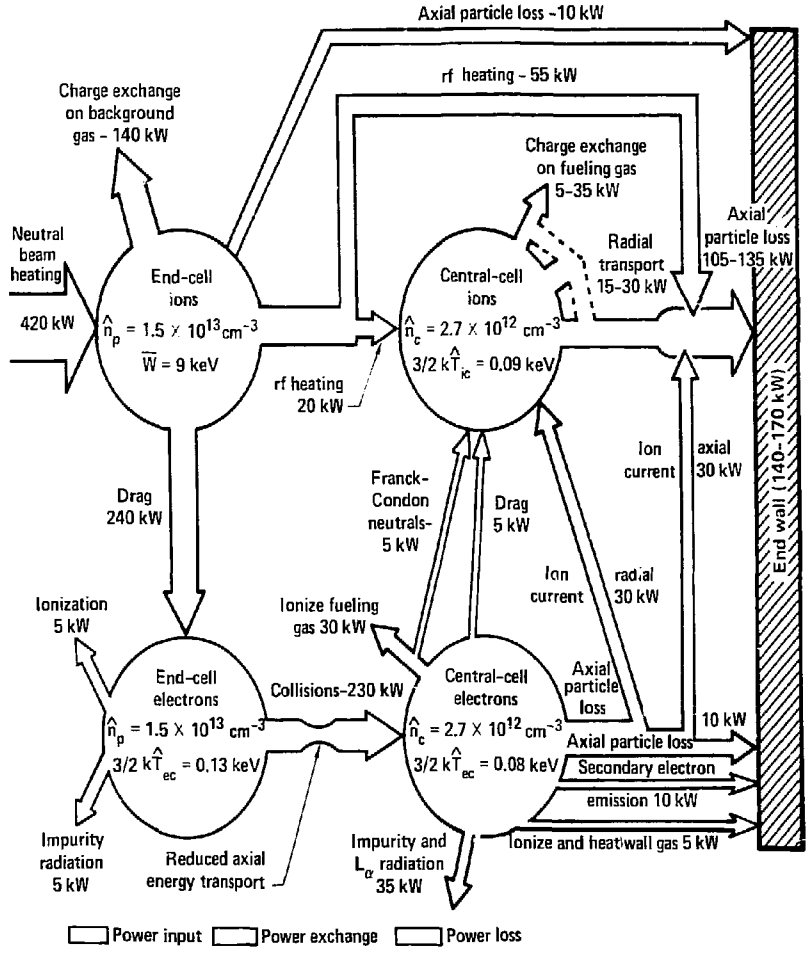

Fig. 1. TMX Power Flow derived from measured plasma parameters.

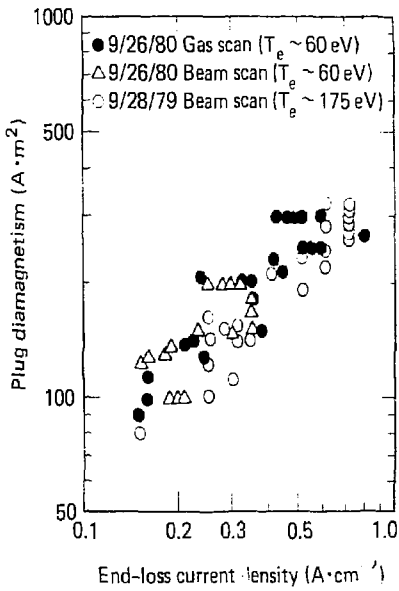

Fig. 2. End-cell diamagnetism versus end-loss current.

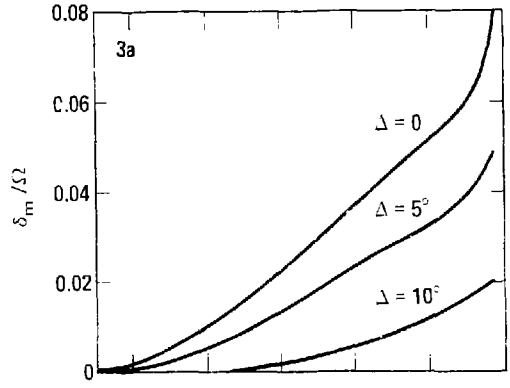

Fig. 3a. The maximum growth rate of AIC instability, in units of the ion cyclotron frequency, as a function of the neutral-beam injection angle ϕ_0 and pitch-angular spread Δ. The uniform 10 keV deuterium plasma has density 4 x 10^{12} cm^{-3} and ℓ = 1, and the magnetic field strength is 10 kG.

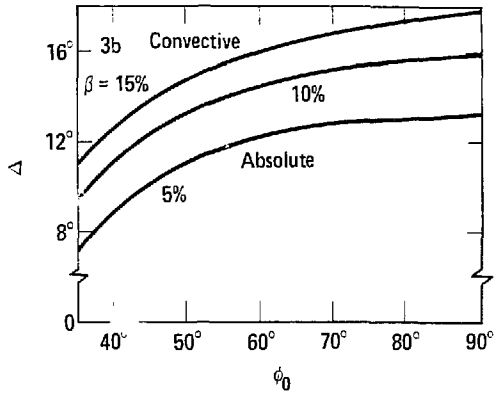

Fig. 3b. Convective-absolute boundaries for AIC instability in a uniform 10 keV hydrogen plasma with $\ell = 2$ in a 5 kG field.

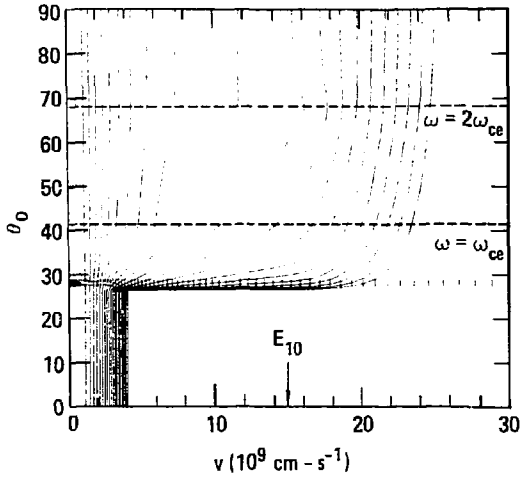

Fig. 4. Contour plot of the electron distribution function in midplane phase space showing that localized ECRH inhibits resonant runaway as evidenced by the rapid decrease in electron density at high energy. The distribution function decreases by a factor 0.58 between contours.

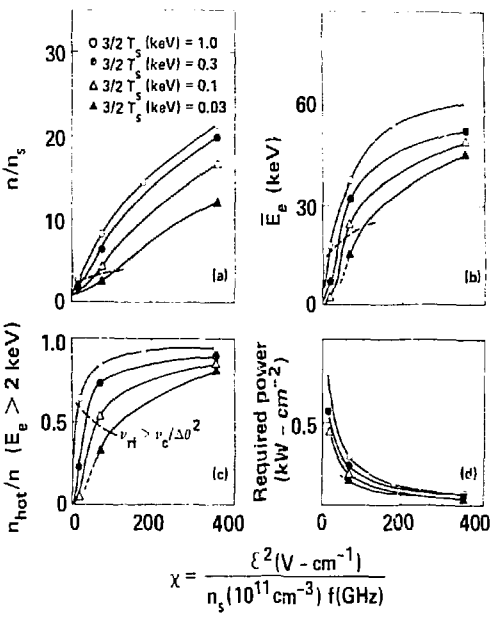

Fig. 5. Plots of (a) plasma density, (b) mean electron energy, (c) fraction of hot electrons, and (d) required ECRH power as a function of χ with relativistic detuning. The source (central cell electron) temperature is T_s. Plasma potential is assumed zero.

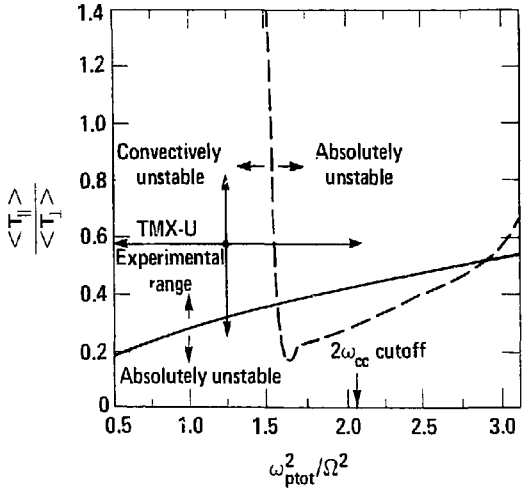

Fig. 6. Convective-absolute instability boundaries for the whistler mode (solid curve) and the upper-hybrid loss-cone mode (dashed curve). TMX-U can obtain over a range of parameters crossing the convective-absolute boundary.

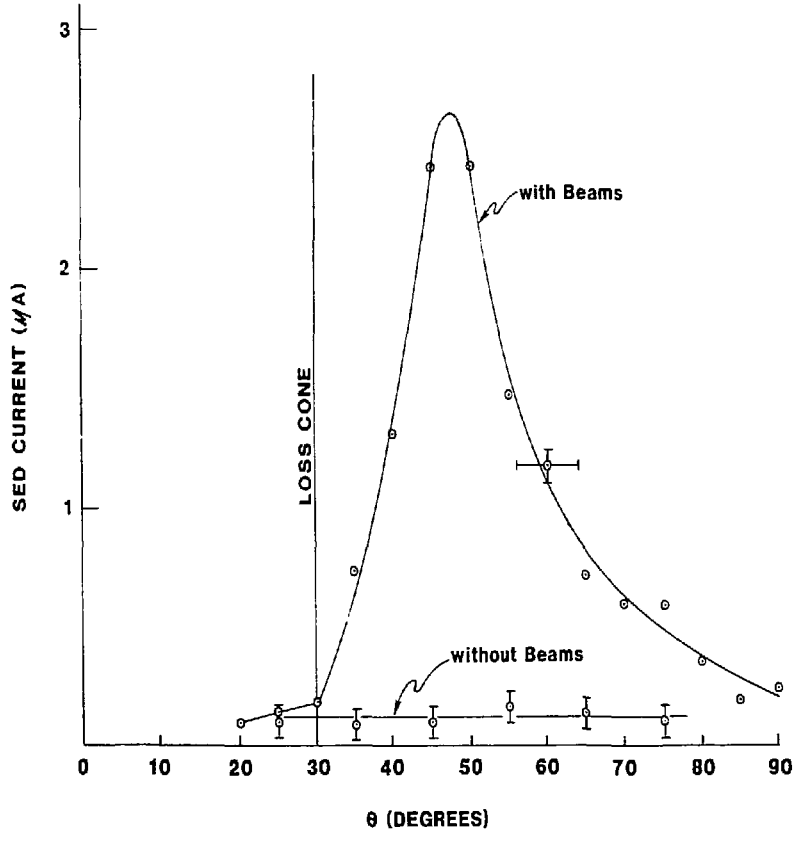

Fig. 7a. Angular distribution of hot end plug ions in TMX-U.

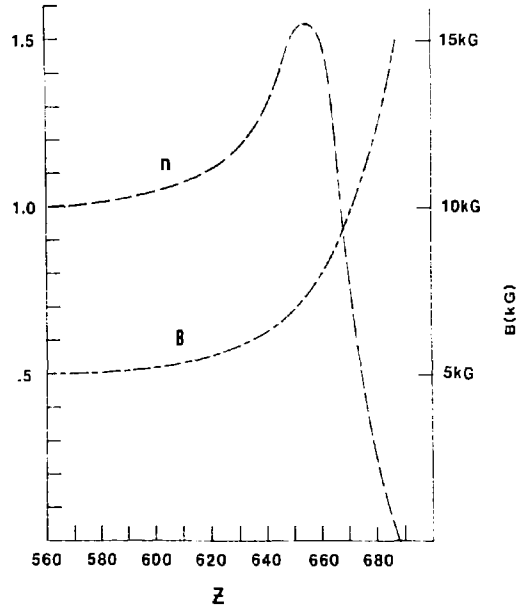

Fig. 7b. Axial density distribution of sloshing ions.